

# Photon-Induced Tunneling in Graphene-Boron Nitride-Graphene Heterostructures

by

Nityan Nair

Submitted to the Department of Physics  
in partial fulfillment of the requirements for the degree of

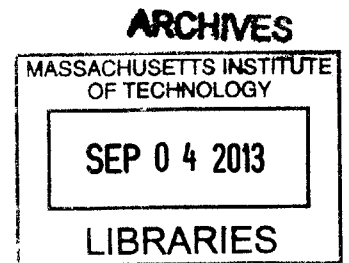
Bachelor of Science in Physics

at the


MASSACHUSETTS INSTITUTE OF TECHNOLOGY

June 2013

© Massachusetts Institute of Technology 2013. All rights reserved.



Author .....

  
Department of Physics  
May 10, 2013

Certified by .....

Pablo Jarillo-Herrero  
Assistant Professor  
Thesis Supervisor

Accepted by .....

Nergis Mavalvala  
Senior Thesis Coordinator, Department of Physics



# Photon-Induced Tunneling in Graphene-Boron Nitride-Graphene Heterostructures

by

Nityan Nair

Submitted to the Department of Physics  
on May 10, 2013, in partial fulfillment of the  
requirements for the degree of  
Bachelor of Science in Physics

## Abstract

Graphene is a material that has generated much interest due to its many unique electronic and optical properties. In this work, we present optoelectronic measurements performed on ultrathin graphene-boron nitride-graphene heterostructures. Scanning photocurrent spectroscopy allows us to explore the tunneling behavior of these devices as a function of both photon energy and bias voltage. Tunneling through the boron nitride insulator is found to be dramatically enhanced by the presence of light, showing a high-bias behavior that can be well described using Fowler-Nordheim tunneling. These measurements indicate that tunneling is dominated by photoexcited positive charge carriers (holes) with an intrinsic barrier height and effective mass of 1.33eV and  $1.19m_e$ , respectively. These numbers agree well with theoretical calculations of the offset between the top of the valence band in boron nitride and the charge neutrality point in graphene, and the effective mass of holes in boron nitride. Moreover, a peak in the conductance was observed at zero bias voltage, indicating the presence of thermionic emission near the charge neutrality point.

Thesis Supervisor: Pablo Jarillo-Herrero  
Title: Assistant Professor



## Acknowledgments

I would like to acknowledge Professor Pablo Jarillo-Herrero for giving me the opportunity to involve myself with research in his group, and for his continual guidance and support, both in and out of the lab. I also want to thank Dr. Nathaniel Gabor and Qiong Ma for their significant contributions to this work and their mentorship and instruction over the past two years. Finally, I would like to thank the entire Jarillo-Herrero group for all their help with the daily challenges of experimental physics, for our many insightful discussions, and for making my research experience both fun and rewarding.



# Contents

<b>1</b>	<b>Introduction</b>	<b>15</b>
1.1	Experimental Overview . . . . .	16
<b>2</b>	<b>Overview of Graphene and Boron Nitride</b>	<b>17</b>
2.1	Crystalline Structure and Electronic Properties . . . . .	17
2.2	Optical Properties of Graphene . . . . .	21
<b>3</b>	<b>Tunneling in Thin-Film Heterostructures</b>	<b>25</b>
3.1	Wentzel-Kramers-Brillouin Approximation . . . . .	25
3.2	Fowler-Nordheim Tunneling . . . . .	27
<b>4</b>	<b>Device Fabrication</b>	<b>31</b>
4.1	CVD Graphene Growth and Transfer . . . . .	31
4.2	Lithography . . . . .	34
4.3	Exfoliation and Transfer . . . . .	35
4.4	Contact Deposition . . . . .	37
<b>5</b>	<b>Measurements and Analysis</b>	<b>39</b>
5.1	Scanning Photocurrent Spectroscopy . . . . .	39
5.2	Resistance Characteristics . . . . .	40
5.3	Tunneling Measurements . . . . .	41
5.4	Comparison to Theory . . . . .	50
5.5	Zero Bias Conductance . . . . .	51





# List of Figures

2-1	An illustration showing the hexagonal atomic structure of graphene (left) and hexagonal boron nitride (right). In graphene, both atoms in the basis are carbon atoms, forming two degenerate sublattices denoted A and B. In boron nitride the two atoms composing the basis are boron and nitrogen, breaking this degeneracy. . . . .	18
2-2	(A) The band structure of graphene calculated using the tight binding model. The conduction and valence bands meet at the $K$ and $K'$ points. (B) An expanded view of the low-energy band structure, corresponding to a conical Dirac dispersion relation. The bottom cone (blue) is in the valence band while the top cone (red) lies in the conduction band. . . . .	19
2-3	A plot showing the resistance of a graphene sample as a function of gate voltage (applied electric field). The peak corresponds to the charge neutrality point. (Image adapted from [6].) . . . . .	20
2-4	The band structure of hexagonal boron nitride, showing a band gap of $\sim 5.2$ eV. For clarity, a schematic of the Brillouin zone is shown to the right. (Image adapted from [9].) . . . . .	21
2-5	A comparison of the roughness of hexagonal boron nitride (left) and silicon oxide (right) measured using an atomic force microscope. The former is more than five times smoother than the latter. (Image adapted from [10].) . . . . .	22

2-6	(A) An illustration showing electron-hole pair generation in graphene for light of different energies. To conserve momentum, electrons and holes must be excited symmetrically about the charge neutrality point. (B) The absorbance of graphene has been measured to be fairly constant across a broad range of photon energies. (Image adapted from [12].)	23
3-1	A schematic showing the tunneling of a high-energy particle through the triangular portion of a potential energy barrier. The low-energy particle, which tunnels through the rectangular portion of the barrier, will have a much lower tunneling probability.	27
4-1	Schematic showing the device geometry. The graphene source and drain electrodes were separated by a thin hBN insulating layer. Both graphene electrodes were connected to two gold contacts (only one shown for clarity). Measurements were performed by applying a voltage to the graphene source and measuring the current collected at the graphene drain. Devices were fabricated on silicon oxide wafers with a conducting silicon back gate (not shown).	32
4-2	An illustration of the CVD graphene transfer process. (a,b) Graphene is grown onto a copper substrate. (c) PMMA is deposited onto the graphene. (d) The copper is chemically etched away from the graphene. (e) The PMMA/graphene stack is placed onto the desired substrate. (f) The PMMA is dissolved leaving only the CVD graphene on the desired substrate.	33
4-3	An overview of the photolithography process showing how CVD graphene (green) is etched into specific geometries. (Image adapted from Rice University: Connexions.)	34
4-4	A CVD graphene bar on a silicon oxide substrate. The graphene has been outlined in white for clarity.	35

4-5	(A) An exfoliated boron nitride flake (blue) on top of a CVD graphene bar (outlined in green). (B) An exfoliated graphene flake on top of the boron nitride flake. The exfoliated graphene is outlined in white for clarity. . . . .	36
4-6	(A) An image of a final device showing two gold contacts to the CVD graphene drain (left and right) and two gold contacts to the exfoliated graphene source (top and bottom). (B) An expanded view of the active region of the device showing the exfoliated graphene source (outlined white) atop the exfoliated boron nitride (blue) atop the CVD graphene drain (outlined green). The purple background is the surface of the silicon oxide wafer. . . . .	38
5-1	A schematic of the experimental apparatus, showing the broadband laser, the scanning mirror, the confocal microscope, and the liquid helium cryostat. . . . .	40
5-2	Resistance characteristics of the graphene source (A) and drain (B) electrodes. Both show a Dirac peak around 0V, implying that extrinsic doping is low. . . . .	41
5-3	A schematic showing the geometry used for tunneling measurements. Tunneling current is collected at the graphene drain while bias is applied to the source and the laser is focused onto the sample. . . . .	41
5-4	A photocurrent image showing the tunneling current measured at the graphene drain as a function of laser position. The active region of the device aligns exactly with the position of the graphene source electrode. $\lambda = 600\text{nm}$ , $P = 100\mu\text{W}$ , $T = 100\text{K}$ , $V_S = 0.5\text{V}$ . . . . .	42
5-5	The tunneling current measured as a function of bias voltage with the laser fixed on the region of highest photoresponse. No tunneling is observed with the laser off, but a large, asymmetric tunneling current is observed with the laser on. . . . .	43

5-6	The tunneling current measured at the graphene drain plotted against photon wavelength (energy) and bias voltage. An asymmetric behavior is observed between the negative and positive bias regions, with the tunneling current exhibiting a sharp peak in photon energy for positive biases. . . . .	44
5-7	Line cuts of the tunneling current measured as a function of photon wavelength (energy) at negative (left) and positive (right) bias voltages. At negative voltages the tunneling current grows monotonically in photon energy. At positive positive voltages, however, the tunneling current exhibits a peak which disperses in bias voltage. . . . .	45
5-8	Schematic showing the shift induced in the Dirac cone of the source electrode when a voltage, $V_S$ , is applied. The presence of a grounded back gate pins the graphene drain, forcing all the shifting to occur in the graphene source. . . . .	46
5-9	(A) A Fowler-Nordheim plot showing $\ln(I(V)/V^2)$ plotted against $1/V$ for various photon wavelengths. Blue dots represent data and red lines represent linear fits. (B) The linear coefficient extracted from the fits in (A) plotted to the two-thirds power. The intrinsic barrier height and effective carrier mass can be extracted from the x-intercept and slope of this line. . . . .	48
5-10	(A) The differential conductance, $dI/dV_S$ , of the tunneling current plotted as a function of photon energy and bias voltage. (B) The position of the positive bias conductance peaks as a function of photon energy and bias voltage. The red line represents the fit to Eq. (5.6). . . . .	49
5-11	Theoretical calculations of the hBN-graphene interface. The red arrow marks the separation between the top of the hBN valence band the charge neutrality point in graphene, which is predicted to be between 1.25 – 2.00 eV. (Image adapted from [21].) . . . . .	50

5-12 The tunneling conductance,  $dI/dV_S$ , plotted on a logarithmic scale, showing a peak at zero bias. This peak persists across a broad range of photon energies. . . . . 51



# Chapter 1

## Introduction

First theoretically studied in 1947 by P. R. Wallace, it was not until recently that graphene was first isolated and observed experimentally [1]. For many decades it was thought that graphene, or other two-dimensional crystals, could not exist since it would not be thermodynamically stable, but in 2003 Andre Geim and Konstantin Novoselov were, for the first time, able to isolated a single sheet of graphene from a bulk graphite crystal [2]. This discovery earned them the Nobel Prize in physics in 2010 and has opened up a new field of condensed matter research. Graphene is a two-dimensional crystal of carbon atoms arranged in a hexagonal lattice. It is part of a larger family of carbon compounds which include buckminsterfullerenes (zero-dimensional), carbon nanotubes (one-dimensional), and graphite (three-dimensional). Although only discovered very recently, graphene has become a very attractive material to study because of its unique properties. Electrons in graphene act as massless Dirac fermions, allowing new physical phenomena to be studied in a controlled environment. Its high carrier mobility has made it a very promising material for producing ultrafast transistors and terahertz antennas. Mechanically, graphene is the strongest known material by weight, but very flexible, making it appealing for use in flexible electronics. Moreover, graphene's large, broadband absorption makes it very promising for use in smaller, more sensitive photodetectors.

## 1.1 Experimental Overview

The many novel properties and applications of graphene have led to an explosion of interest in the field. In this work, we study the optoelectronic properties of graphene heterostructures. Specifically, we fabricated graphene-boron nitride-graphene devices in order to study photon-induced tunneling through the insulating boron nitride barrier. Measurements were performed using a confocal scanning photocurrent microscopy setup that allowed us to measure the photon-induced tunneling current as a function of position and photon energy. The purpose of this project was to determine whether photons could be used to enhance tunneling in these types of device and, if so, to use this technique to measure properties of the graphene-boron nitride interface. If photons are indeed able to enhance tunneling in this type of system, it opens up the possibility of using graphene-insulator-graphene heterostructures to make new, ultrasensitive photodetectors with very high signal to noise ratios. Moreover, this technique of using light to modify tunneling behavior could be used as a probe to study the properties of material interfaces, in this case the graphene-boron nitride interface.



# Chapter 2

## Overview of Graphene and Boron Nitride

### 2.1 Crystalline Structure and Electronic Properties

Both graphene and hexagonal boron nitride (hBN) are composed of hexagonal Bravais lattices with two-atom bases. In graphene, both of the atoms in the basis are carbon atoms. This particular symmetry leads to unique electronic properties which have been the subject of much excitement in the field. In boron nitride, on the other hand, the two atoms in the basis are boron and nitrogen, as shown in Figure 2-1. Although boron nitride can be isolated into a monolayer, like graphene, this different basis structure leads to very different electronic and optical properties.

In the past several years it has been observed that graphene's electronic properties (mobility, extrinsic doping, etc.) can be dramatically improved by placing it on an hBN substrate [3]. This improvement comes as a result of hBN's two dimensional planar structure, which gives the material an ultraflat surface, free of charge traps and dangling bonds. This has led to a great deal of interest in using hBN as a substrate and dielectric layer in graphene devices, and has even been used in transport measurements on graphene-hBN-graphene tunneling junctions [4].

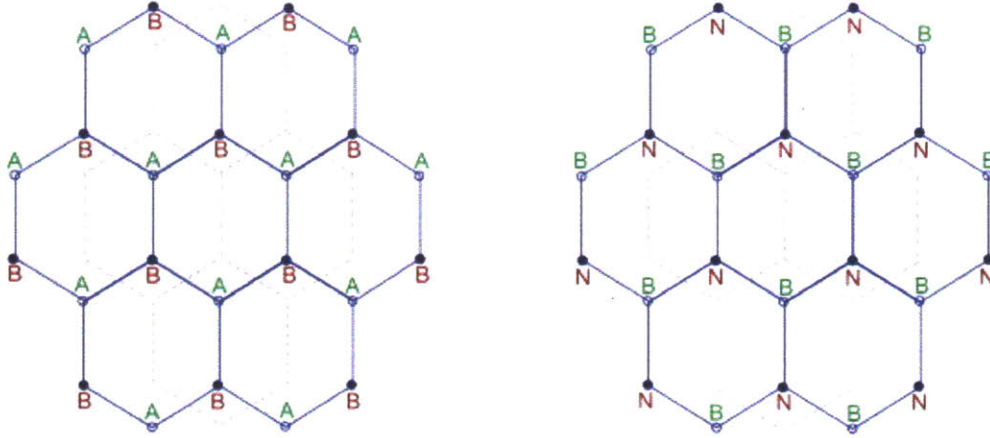


Figure 2-1: An illustration showing the hexagonal atomic structure of graphene (left) and hexagonal boron nitride (right). In graphene, both atoms in the basis are carbon atoms, forming two degenerate sublattices denoted A and B. In boron nitride the two atoms composing the basis are boron and nitrogen, breaking this degeneracy.

The atomic orbitals in both graphene and hBN are  $sp^2$  hybridized and form  $\sigma$  bonds with their nearest neighbors. The remaining  $p_z$  orbital forms  $\pi$  bonds with its nearest neighbors and it is these  $\pi$  bonds that form the relevant electronic band structure at low energies. For graphene, the electronic band structure can be calculated to a surprisingly good approximation using the tight binding model. The tight binding model assumes that electrons in the  $\pi$  bonds are strongly localized to lattice sites. The overall wavefunction of the system is then given by the superposition of these localized bonds, weighted by a periodic phase of  $e^{i\mathbf{k}\cdot\mathbf{R}}$ . The phase factor comes from Bloch's theorem and arises from the periodicity of the lattice. Once the wavefunction has been approximated in this manner, the expectation value of the energy (as a function of wavevector) can be calculated using a tight-binding hamiltonian with nearest neighbor interactions.

The band-structure calculated for graphene using the tight binding approximation is shown in Figure 2-2A [5]. The most important feature to note is that there is no band-gap in this material. Graphene is a semimetal where the valence and conduction bands meet at the  $K$  and  $K'$  points. Moreover, at low energies, electrons have a linear, relativistic dispersion relation, more commonly referred to as a Dirac cone. Expanding the band structure about the  $K$  and  $K'$  points, the dispersion relation

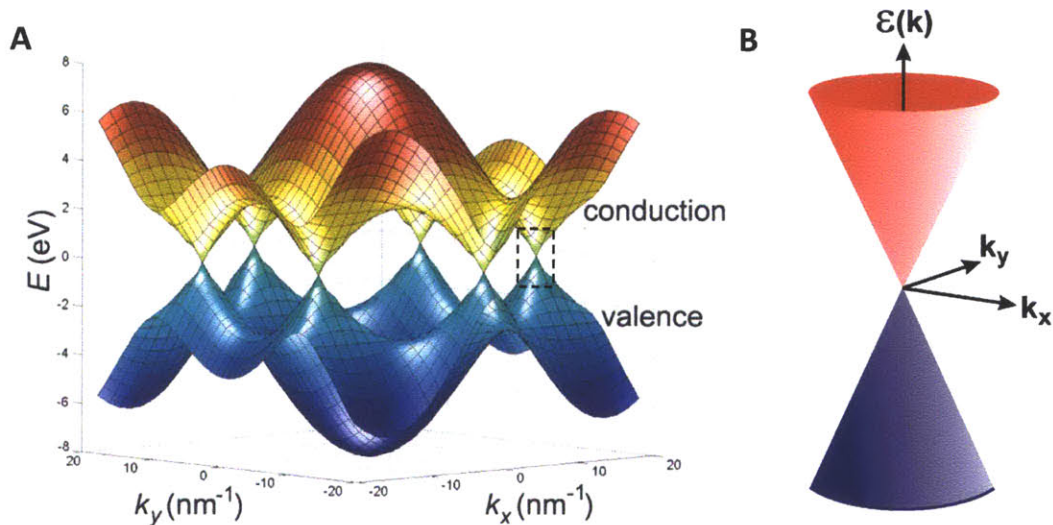


Figure 2-2: (A) The band structure of graphene calculated using the tight binding model. The conduction and valence bands meet at the  $K$  and  $K'$  points. (B) An expanded view of the low-energy band structure, corresponding to a conical Dirac dispersion relation. The bottom cone (blue) is in the valence band while the top cone (red) lies in the conduction band.

becomes  $E_{\pm} \approx v_F |\mathbf{q}|$ , where  $\mathbf{q}$  is the momentum measured with respect to these points. Electrons in this system behave as massless Dirac fermions and travel with a constant Fermi velocity,  $v_F$ , which has been measured to be  $v_F \approx 1 \times 10^6 \text{ m/s}$  [5]. The Dirac cone dispersion relation is shown in Figure 2-2B.

The conical Dirac dispersion of graphene leads to many interesting and novel phenomena in graphene devices. One of these phenomena is that current in graphene can be carried by either negative or positive charge carriers (electrons or holes) [6]. The type of charge carrier, as well as the carrier density, can be tuned through the application of a transverse electric field to the sample. In zero electric field, the Fermi energy in intrinsic graphene lies at the charge neutrality point (sometimes referred to as the Dirac point), the crossing point of the Dirac cone. At this point, the charge carrier concentration is zero. Applying an electric field perpendicular to the graphene sheet can induce charge carriers to flow into the graphene from the contact electrodes, changing the carrier concentration and therefore the Fermi energy. This procedure, known as field effect gating, can also be used to shift the charge carriers from electrons to holes, or vice versa, as the Fermi energy is moved through the charge neutrality

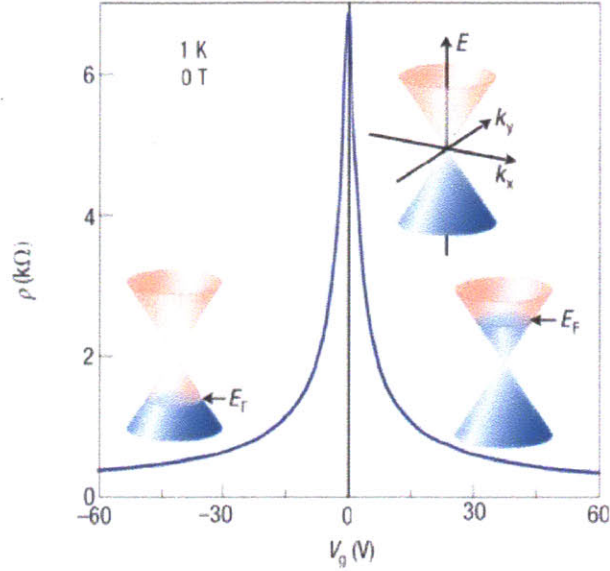


Figure 2-3: A plot showing the resistance of a graphene sample as a function of gate voltage (applied electric field). The peak corresponds to the charge neutrality point. (Image adapted from [6].)

point. Tuning the material from n-type doped to p-type doped through the charge neutrality point causes a peak in the resistance of the sample since the carrier density will go to zero. This peak, known as a Dirac peak, can be easily measured (see Figure 2-3). From the shape of the Dirac peak, the mobility of charge carriers in the material can be calculated.

Besides the ambipolar tunability of charge carriers there are many other unique and interesting phenomena that arise from graphene's conical dispersion. Although it will not be discussed here, the anomalous quantum hall effect in graphene, analogous to the integer quantum hall effect in conventional materials, has generated much interest in recent years [7]. Moreover, graphene has the unique property that charge carriers which encounter a potential energy barrier in the material will tunnel through the barrier with a probability of one for certain special incident angles [8]. This phenomenon, known as Klein Tunneling, arises from the Dirac nature of electrons in graphene and is only one of many novel quantum phenomena that may be observable using this material.

Although hexagonal boron nitride has a very similar lattice structure to graphene,

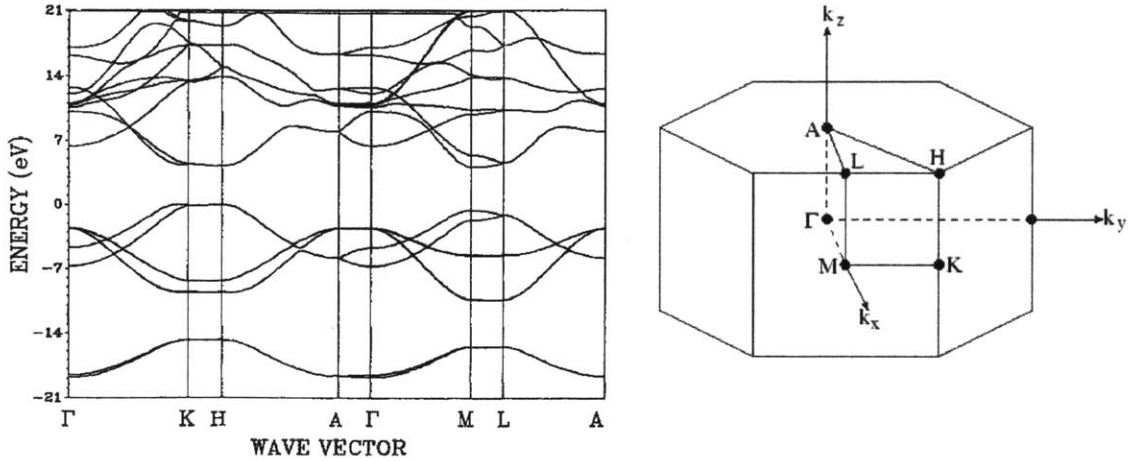


Figure 2-4: The band structure of hexagonal boron nitride, showing a band gap of  $\sim 5.2$  eV. For clarity, a schematic of the Brillouin zone is shown to the right. (Image adapted from [9].)

its non-degenerate, two-atom basis, yields a very different electronic band structure, as depicted in Figure 2-4. Unlike graphene, which is a zero-gap semi-metal, boron nitride acts as an insulator with a very large band gap of  $\sim 5.2$  eV, and electrons (holes) at the bottom (top) of the conduction (valence) band behave as massive, non-relativistic fermions with a quadratic dispersion relation [9]. What makes boron nitride a very interesting material, however, is that, when cleaved properly, it forms a very flat, pristine surface and can be used as a substrate for other thin-film materials. A comparison of the roughness of silicon oxide and hBN is shown in Figure 2-5. It has recently been observed that graphene sample quality can be improved dramatically when deposited onto hBN [10]. This makes boron nitride an ideal material to be used as a tunneling barrier in graphene systems.

## 2.2 Optical Properties of Graphene

Graphene has many optical properties arising from its band structure which make it a very promising material in optoelectronics applications. First, because graphene has no band gap, it can absorb light via interband transitions across a broad range of spectra. This process is illustrated in Figure 2-6, and leads to an absorption spectrum

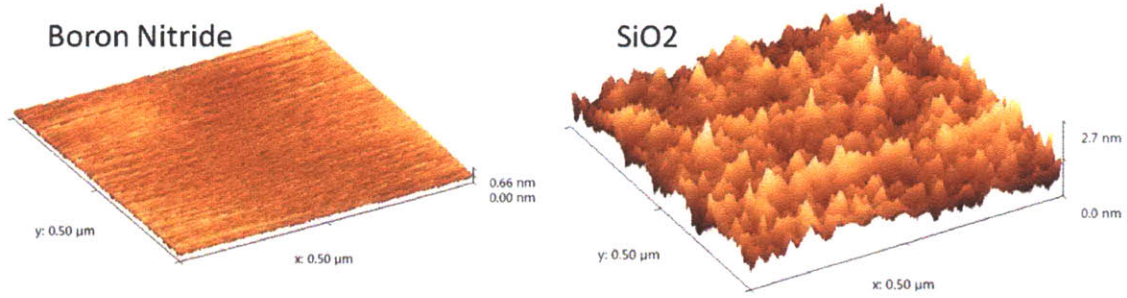


Figure 2-5: A comparison of the roughness of hexagonal boron nitride (left) and silicon oxide (right) measured using an atomic force microscope. The former is more than five times smoother than the latter. (Image adapted from [10].)

that is relatively flat from the mid-infrared to the near ultraviolet (with a peak at 270nm due to a van Hove singularity in the density of states) [11]. Because graphene can be easily gated using field effect gating (see Section 2.1), low-energy interband transitions can be Pauli blocked, allowing tunability of graphene’s absorption spectrum in the infrared.

Another important optical property of graphene is the presence of a strong hot-carrier effect [13]. When electrons in graphene are optically excited, they form an energetic, non-equilibrium carrier population in the conduction band, leaving a corresponding distribution of holes in the valence band. These distributions cool through two primary mechanisms: fast, intraband electron-electron interactions mediated by optical phonons, and slow electron-hole interband interactions mediated by acoustic phonons. The first cooling mechanism, electron-electron interactions, equilibrates quickly, heating the optical phonon bath to the electronic temperature, still far above the lattice temperature. The second cooling mechanism, electron-hole interactions, should, in theory cool the electronic system back down to the lattice temperature. In practice, however, it has been found that this process must be mediated by acoustic phonons (to conserve momentum) and these acoustic phonons act as a bottleneck, especially near the charge neutrality point. As a result, this cooling process in graphene has a very long timescale, meaning that excited electrons in the system remain hot.

The hot-carrier effect makes graphene a very enticing material for use in energy applications. Because electrons stay hot in the system, they can travel significant

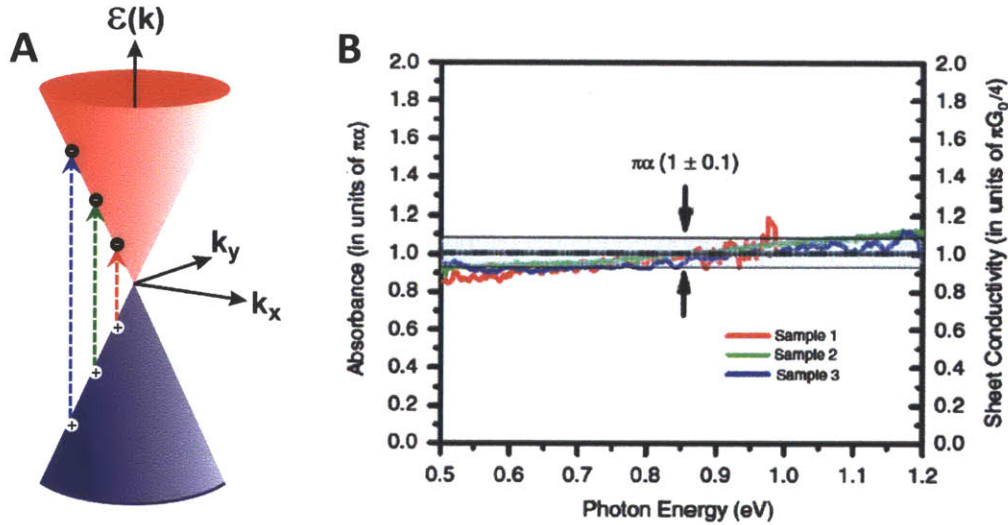


Figure 2-6: (A) An illustration showing electron-hole pair generation in graphene for light of different energies. To conserve momentum, electrons and holes must be excited symmetrically about the charge neutrality point. (B) The absorbance of graphene has been measured to be fairly constant across a broad range of photon energies. (Image adapted from [12].)

distances ( $> 2\mu\text{m}$ ) without losing energy. This highly non-local photoresponse is predicted to increase the efficiency of energy-harvesting devices beyond the standard limits [14]. This improvement arises from the fact that the elevated carrier temperature leads to a substantially higher Carnot efficiency limit. Moreover, hot carriers are predicted to enhance thermionic emission, potentially allowing for hybrid photon-enhanced thermionic emission devices, which should offer large efficiency improvements over conventional photovoltaic or photothermal devices [15]. In essence, these devices use thermal energy to enhance the emission of photo-generated charge carriers over a barrier, thereby driving a current. If these types of devices can be realized, then they promise to have a large impact on the way we generate energy.





# Chapter 3

## Tunneling in Thin-Film Heterostructures

Tunneling is a quantum mechanical phenomenon by which a particle can travel through a potential energy barrier that, classically, it would not have been able to cross. In this work, we observed the tunneling of electrons through a thin insulating layer of boron nitride. The band gap of the boron nitride served to create a potential energy barrier for electrons in the graphene sheets. Under normal conditions, the boron nitride barrier height is too high for there to be any significant probability for electrons to tunnel across [4]. When light was shown onto the electrons, however, they were excited into higher energy states, decreasing the effective barrier height and increasing the tunneling probability to the point where a significant tunneling current could be observed.

### 3.1 Wentzel-Kramers-Brillouin Approximation

The Wentzel-Kramers-Brillouin (WKB) approximation is the most basic description of a quantum mechanical particle tunneling through a slowly varying potential. It is a semiclassical approximation in which the particle's wavefunction is propagated as a decaying exponential through a potential barrier in order to calculate the probability of measuring the particle on the other side. In order to derive the WKB approxi-

mation to the tunneling probability, we start with the time-independent Schrodinger equation, which in one dimension is given by

$$-\frac{\hbar^2}{2m^*} \frac{d^2\Psi(x)}{dx^2} + V(x)\Psi = E\Psi(x) \quad (3.1)$$

for non-relativistic particles, such as electrons in the bands of a semiconductor. Here,  $m^*$  is the effective mass of the particle,  $E$  is its energy,  $\Psi(x)$  is the wavefunction, and  $V(x)$  is the shape of the potential energy barrier. This equation can be rewritten as

$$\frac{d^2\Psi(x)}{dx^2} = \frac{2m^*(V(x) - E)}{\hbar^2} \Psi(x) \quad (3.2)$$

For an arbitrary  $V(x)$ , Eq. (3.2) is a very non-trivial equation to solve. Progress, however, can be made using the WKB approximation, which essentially assumes that the potential barrier varies very slowly compared to the de Broglie wavelength of the particle. If we assume that  $V(x)$  is slowly varying over some small distance  $dx$ , then the solution to Eq. (3.2) can be written as

$$\Psi(x + dx) = \Psi(x) \exp \left[ -\sqrt{\frac{2m^*(V(x) - E)}{\hbar^2}} dx \right] \quad (3.3)$$

Once again assuming that the potential is slowly varying, the above equation can be integrate across the potential barrier to find that

$$\Psi(L) = \Psi(0) \exp \left[ -\int_0^L \sqrt{\frac{2m^*(V(x) - E)}{\hbar^2}} dx \right] \quad (3.4)$$

where  $L$  is the length of the region where the potential,  $V(x)$ , exceeds the particle energy,  $E$ . To find the probability of a single particle tunneling through this barrier, one simply compares the modulus squared of the wavefunction to the left of the barrier to the modulus squared of the wavefunction to the right of the barrier. In the WKB approximation the probability for a particle to pass through a potential barrier of the

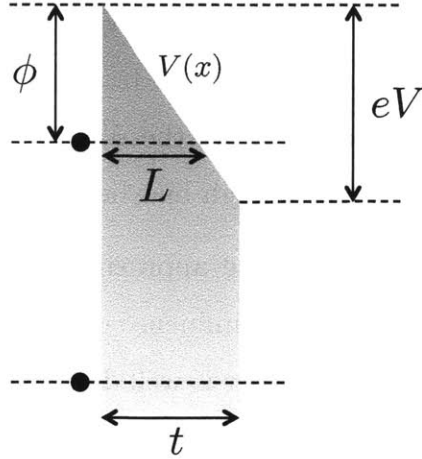


Figure 3-1: A schematic showing the tunneling of a high-energy particle through the triangular portion of a potential energy barrier. The low-energy particle, which tunnels through the rectangular portion of the barrier, will have a much lower tunneling probability.

form  $V(x)$  becomes

$$T = \frac{|\Psi(L)|^2}{|\Psi(0)|^2} = \exp \left[ -2 \int_0^L \frac{\sqrt{2m^*(V(x) - E)}}{\hbar} dx \right] \quad (3.5)$$

The WKB approximation has been tested extensively and has been found to work very well in cases where potentials are slowly varying or constant and many-body dynamics do not play a large role [16]. Unfortunately, WKB alone is not sufficient to describe the tunneling phenomena observed in the devices measured here and a more advanced tunneling theory, known as Fowler-Nordheim tunneling is needed.

## 3.2 Fowler-Nordheim Tunneling

While WKB accurately describes the direct tunneling of particles through potential barriers, tunneling through an insulator in the presence of an electric field is a more complicated process and cannot be explained by WKB alone. The primary difference arises from the the fact that, at high electric fields, the potential barrier produced by the band gap of an insulator is tilted, forming a triangular barrier. Moreover, as is shown in Figure 3-1, given a sufficiently large energy, charge carriers traveling through

an insulator will tunnel through the triangular barrier and into the conduction band of the material, where they will undergo ballistic transport to the drain electrode. The Fowler-Nordheim tunneling model builds on the WKB approximation, incorporating this region of ballistic transport in the high bias limit [17].

The band gap of an insulator can be approximated as a rectangular potential barrier, which becomes tilted under the influence of an electric field. The tunneling probability through this triangular barrier is well-described by the WKB approximation where  $V(x)$  and  $L$  in Eq. (3.5) both become functions of the applied electric field. Since the applied electric field is known,  $V(x)$  and  $L$  can be solved for. Applying Eq. (3.5), one obtains the following expression for the tunneling probability through the triangular portion of the barrier

$$T_{FN} = \exp \left[ -\frac{4t\sqrt{2m^*}\phi^{3/2}}{3e\hbar V} \right] \quad (3.6)$$

Here  $t$  is the thickness of the insulating barrier layer,  $m^*$  is the effective mass of charge carriers in the insulator,  $V$  is the bias voltage applied across the insulator, and  $\phi$  is the effective height of the potential energy barrier at zero applied field.

Once a charge carrier tunnels through the triangular barrier, it ends up in the conduction band of the insulator, from where it travels to the drain electrode via ballistic transport. In the low temperature limit, this process results in a prefactor to the tunneling probability provided by the WKB expression [17]. The resulting expression for the total tunneling current becomes

$$I(V) = \frac{e^3 m_0 A V^2}{16\pi^2 \hbar m^* \phi t^2} \exp \left[ -\frac{4t\sqrt{2m^*}\phi^{3/2}}{3e\hbar V} \right] \quad (3.7)$$

where  $m_0$  is the rest mass of a free electron and  $A$  is the effective tunneling area.

Eq. (3.7) can be rewritten in a form that is much more useful when fitting experimental data. Rearranging terms and taking the natural logarithm, one obtains that

$$\ln \frac{I(V)}{V^2} = \ln \left[ \frac{e^3 m_0 A}{16\pi^2 \hbar m_n^* \phi t^2} \right] - \frac{4t\sqrt{2m_n^*}\phi^{3/2}}{3e\hbar} \frac{1}{V} \quad (3.8)$$

In this form, it is very clear that  $\ln(I(V)/V^2)$  is linear in  $1/V$ . If Fowler-Nordheim tunneling accurately describes the tunneling mechanism in a sample, then measuring the  $I - V$  curve of the sample and plotting  $\ln(I(V)/V^2)$  against  $1/V$  should yield a straight line. From this line the effective barrier height,  $\phi$ , or the effective carrier mass,  $m^*$ , can be determined. In the graphene-boron nitride-graphene heterostructures measured here, Fowler-Nordheim tunneling was used to explain the tunneling behavior and numerical fits were used to extract both the effective barrier height and the effective carrier mass.



# Chapter 4

## Device Fabrication

In order to study tunneling in graphene-boron nitride-graphene heterostructures, nano-scale devices were fabricated using modern clean room techniques. The basic device geometry is shown in Figure 4-1. Our devices consisted of a long, atomically thin drain electrode made from chemical vapor deposited graphene. An exfoliated hexagonal boron nitride (hBN) tunnel barrier was deposited on top of the graphene drain followed by an exfoliated graphene source electrode. The entire device was fabricated on a degenerately doped silicon substrate with a  $285\text{nm}$  surface layer of silicon oxide and a conducting silicon back gate. The active area (area covered by all three layers) of typical devices was  $\sim 10\mu\text{m}^2$  and the thickness of the hBN tunneling barriers ranged from  $7\text{nm}$  to  $24\text{nm}$ . The device geometry described above allowed us to place a bias voltage across the hBN layer and measure the tunneling current produced under various illumination conditions.

### 4.1 CVD Graphene Growth and Transfer

Chemical Vapor Deposition (CVD) is a process by which atoms are deposited onto a substrate under conditions such that they will crystallize into a desired thin-film material. In this case, the drain graphene layer was produced using chemical vapor deposition of carbon onto a copper substrate. Thin copper films ( $\sim 20\mu\text{m}$ ) were placed into a sterile quartz growth furnace and heated to  $\sim 1000^\circ\text{C}$  under low vacuum.

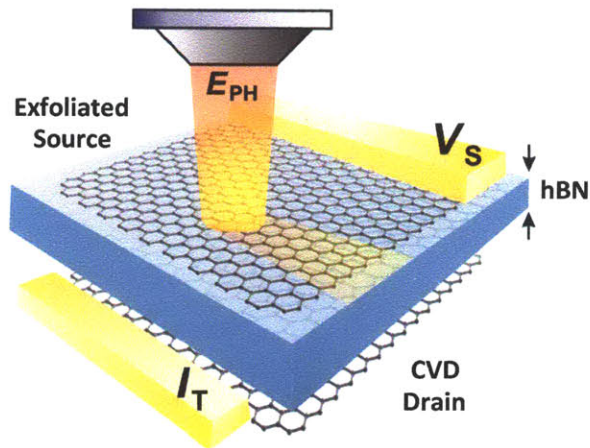


Figure 4-1: Schematic showing the device geometry. The graphene source and drain electrodes were separated by a thin hBN insulating layer. Both graphene electrodes were connected to two gold contacts (only one shown for clarity). Measurements were performed by applying a voltage to the graphene source and measuring the current collected at the graphene drain. Devices were fabricated on silicon oxide wafers with a conducting silicon back gate (not shown).

Hydrogen and methane gas was then passed over the film. The hydrogen serves to catalyze a reaction by which the methane molecules separate and the carbon atoms are adsorbed into the surface of the copper substrate. Under the proper growth conditions the carbon atoms can be induced to form a monolayer at the surface of the copper. When the copper substrate is then rapidly cooled back down to room temperature, the carbon monolayer crystallizes into a layer of graphene. The end result of this process is a copper film covered by a CVD graphene monolayer.

Once the CVD graphene has been grown on the copper substrate, it still has to be transferred to the silicon wafer onto which the actual device will be built. The transfer process is outlined in Figure 4-2. A poly(methyl methacrylate) (PMMA) film is spun onto the graphene, holding it in place while the copper substrate is chemically etched away using iron (III) chloride. Once the copper has been completely etched, the PMMA film with the CVD graphene can be removed from the iron (III) chloride solution and is rinsed several times with hydrochloric acid and water to remove any contaminants. The PMMA membrane is then placed onto a doped silicon wafer with a 285nm top-layer of silicon oxide with the graphene-side in contact with the substrate.



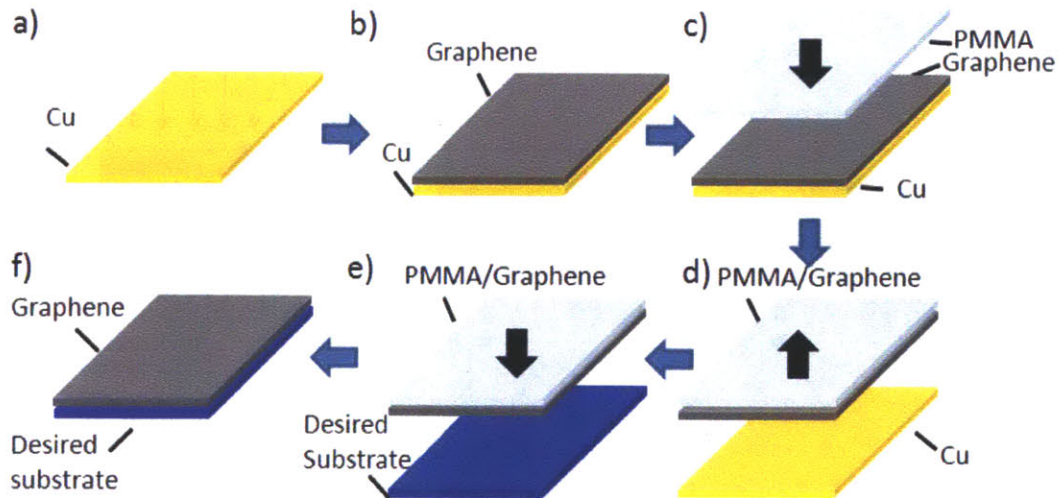


Figure 4-2: An illustration of the CVD graphene transfer process. (a,b) Graphene is grown onto a copper substrate. (c) PMMA is deposited onto the graphene. (d) The copper is chemically etched away from the graphene. (e) The PMMA/graphene stack is placed onto the desired substrate. (f) The PMMA is dissolved leaving only the CVD graphene on the desired substrate.

The PMMA is dissolved using acetone, leaving the CVD graphene layer on top of the silicon substrate. Once on the substrate, the graphene can be patterned and etched in order to build devices.

There are several advantages and drawbacks that come from using CVD graphene instead of the more traditional exfoliated graphene for the drain electrode. Unlike mechanical exfoliation, chemical vapor deposition can be used to grow large-area ( $> 1\text{cm}^2$ ) graphene sheets. This makes it easy to pattern and fabricate en masse. Moreover, having a large drain electrode makes transferring the insulating layer and the source electrode during subsequent fabrication steps much easier, allowing for a faster fabrication cycle when building devices.

CVD graphene, however, also has several drawbacks, most notably its lower quality. CVD samples are generally found to have lower mobility and higher doping than their exfoliated counterparts [18]. This stems from the fact that the CVD growth process inherently produces multi-domain crystals. Where these domains meet, grain boundaries form: regions that are particularly chemically active and tend to form bonds to stray contaminants. As a result, these boundaries form potential barriers

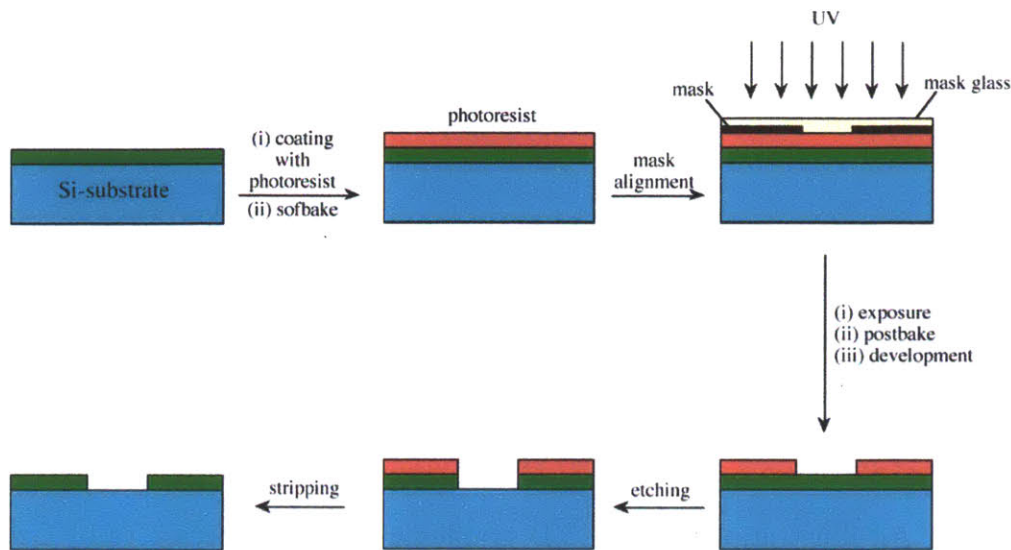


Figure 4-3: An overview of the photolithography process showing how CVD graphene (green) is etched into specific geometries. (Image adapted from Rice University: Connexions.)

and scatter charge carriers, reducing bulk carrier mobility [19].

## 4.2 Lithography

The CVD graphene drain electrodes were patterned using a combination of photolithography and reactive ion etching (RIE). Once transferred to a silicon oxide substrate, the CVD graphene layer is coated with the negative photoresist AZ 5214. When exposed to ultraviolet light, AZ 5214 molecules become activated, allowing them to be easily removed by chemical processes. By using a mask to selectively expose regions on the sample, patterns can be engraved into the AZ 5214 layer. The graphene no longer covered by photoresist is etched away using a reactive ion oxygen plasma, leaving the mask pattern imprinted into the CVD graphene. This process is summarized in Figure 4-3. In these specific devices, the CVD graphene was patterned into  $100\mu\text{m}$  long,  $10\mu\text{m}$  wide bars, to serve as drain electrodes (see Figure 4-4).

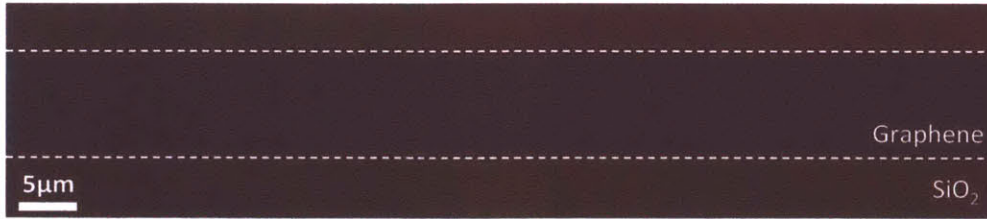


Figure 4-4: A CVD graphene bar on a silicon oxide substrate. The graphene has been outlined in white for clarity.

### 4.3 Exfoliation and Transfer

Although chemical vapor deposition allows one to produce large-area sheets of a material, the technique of mechanical exfoliation generally produces much higher quality samples by cleaving naturally formed bulk crystals. Because of this, it was used to produce both the boron nitride tunneling barrier and the graphene source electrode.

The process of mechanical exfoliation begins with the preparation of the substrate onto which the sample will be exfoliated, imaged, and transferred from. We begin with a macroscopic layer of polydimethylsiloxane (PDMS) resting atop a glass slide. The PDMS serves as a flexible support structure for the exfoliated flakes. The stack is then covered with a piece of clear packing tape to serve as a sticking layer for the poly(methyl methacrylate) (PMMA) membrane that is deposited onto it. The desired material can then be exfoliated onto the PMMA membrane, which will be held rigidly in place by the PDMS layer below. The entire stack, PMMA, tape, PDMS, and the glass slide, is clear, allowing exfoliated flakes to be optically imaged from either the top or the bottom.

Exfoliation of the graphene and boron nitride was done using laboratory-grade sticky-tape. Once the crystal has been exfoliated several times onto the tape, the tape with the exfoliated crystal fragments is pressed onto the PMMA membrane of the transfer stack and removed, leaving exfoliated crystal flakes behind. Using an optical microscope, boron nitride flakes (or monolayer graphene flakes) can be identified for transfer.

Once desired flakes are identified, they, along with the PMMA/PDMS substrate,

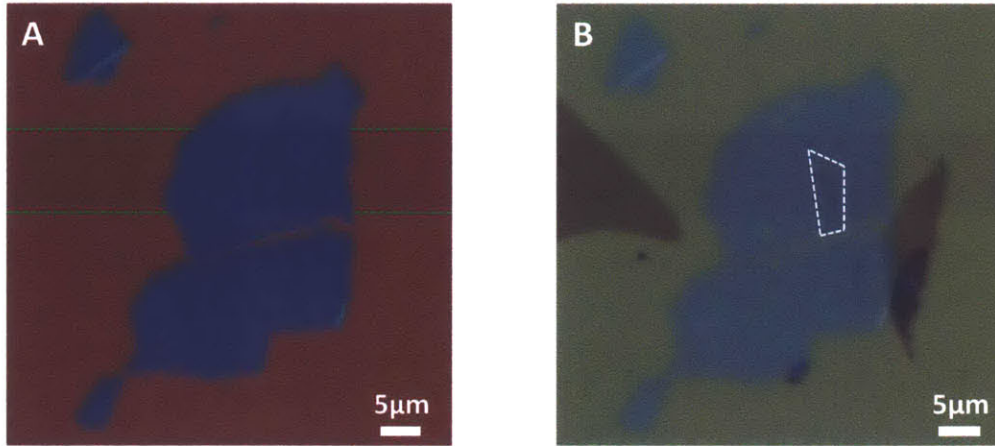


Figure 4-5: (A) An exfoliated boron nitride flake (blue) on top of a CVD graphene bar (outlined in green). (B) An exfoliated graphene flake on top of the boron nitride flake. The exfoliated graphene is outlined in white for clarity.

are cut from the glass slide and remounted. The result is a small ( $\sim 1\text{mm}^2$ ) stack of PMMA/tape/PDMS with the desired exfoliated flake on top, affixed to a glass slide. The entire device is then inverted and the glass slide is mounted into a 3-axis micropositioner. The target wafer is mounted to a heated vacuum chuck below the glass slide. Since the glass/PDMS/PMMA stack is transparent, the exfoliated flake can still be located using a microscope and, using the 3-axis micropositioner, can be aligned to features on the wafer.

Once flakes are aligned to features on the wafer, the PMMA/PDMS stack is lowered until the PMMA layer with the exfoliated flake is in contact with the wafer. The wafer is then heated to  $135^\circ\text{C}$ , causing the PMMA to stick to the substrate and separate from the PDMS. The PDMS is then lifted away, leaving the PMMA layer with the exfoliated flake stuck to the wafer. The PMMA is removed using acetone, leaving only the exfoliated flake on the wafer. In this manner, exfoliated flakes can be reliably aligned and transferred to silicon oxide wafers with precision. This exfoliation and transfer process was used to transfer the hexagonal boron nitride tunneling layer onto the CVD graphene drain electrode, and the exfoliated graphene source electrode onto the boron nitride. The results of these steps are shown in Figure 4-5.

## 4.4 Contact Deposition

Once the graphene electrodes and the hBN layer were in place, the only remaining step was to create electrical contacts to the device. Since graphene flakes are too small and fragile to be contacted with wires directly, chrome/gold was evaporated onto the device to contact the graphene directly and form pads onto which wires could be bonded. This was done using electron beam lithography to create the contact patterns and electron beam deposition to fill the patterned areas with chrome/gold.

Electron beam lithography is very similar to photolithography (see Section 4.2). Instead of using a resist that is sensitive to light, a resist that is sensitive to high-energy electrons is used instead. The sample is coated in this resist (in our case PMMA) and the electron beam is scanned across the device, turning on only in areas to be written (much like a serial printer). Unlike in photolithography, no mask has to be made for this process, allowing for much faster turnaround times for new contact designs. Moreover, since the wavelength of the electrons is much less than that of ultraviolet light, smaller, nano-scale features can be produced. The downside of electron beam lithography, however, is that because patterns are written line-by-line, producing a single device often takes on the order of hours (compared to minutes for photolithography). Once the pattern has been written using the electron beam, the exposed areas of the resist are then removed through chemical processes, leaving the desired pattern engraved into the sample.

Once the contact pattern was engraved into the PMMA layer, chrome/gold was deposited onto the device to form the contacts. This was done using electron beam deposition. In essence, a beam of electrons is used to heat up a sample of the desired deposition material under high vacuum until it begins to sublime. The metal atoms deposit themselves onto the sample, filling in the patterned areas of the PMMA membrane. Using chemical means the PMMA is then removed from the sample, leaving a layer of chrome/gold only where the pattern was. In this manner, nano-scale contacts can be fabricated for both the source and drain graphene electrodes. A  $\sim 5\text{nm}$  layer of chrome was deposited first to act as a sticking layer for the gold, after

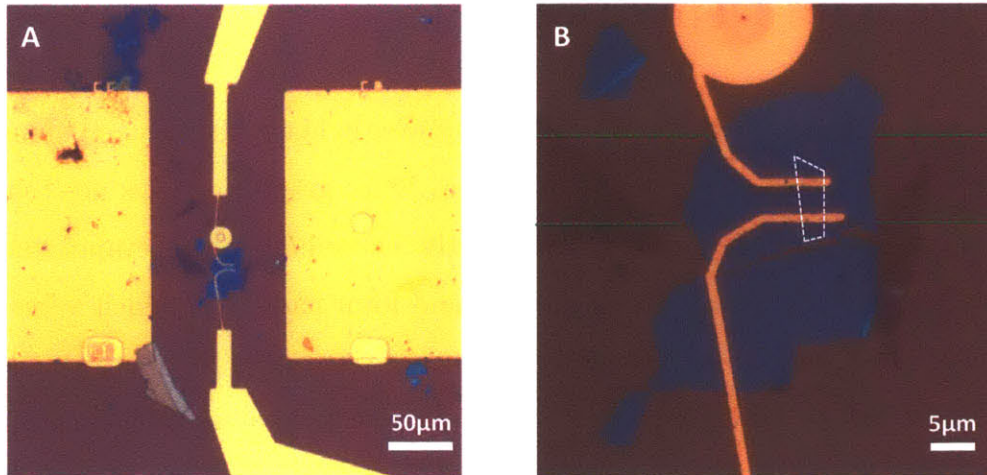


Figure 4-6: (A) An image of a final device showing two gold contacts to the CVD graphene drain (left and right) and two gold contacts to the exfoliated graphene source (top and bottom). (B) An expanded view of the active region of the device showing the exfoliated graphene source (outlined white) atop the exfoliated boron nitride (blue) atop the CVD graphene drain (outlined green). The purple background is the surface of the silicon oxide wafer.

which a  $\sim 60\text{nm}$  layer of gold was deposited to form the electrical contacts. Each graphene electrode was contacted in two places, allowing for the resistance of each to be measured independently using a two-probe measurement. An optical image of a final device is shown in Figure 4-6.

# Chapter 5

## Measurements and Analysis

### 5.1 Scanning Photocurrent Spectroscopy

Graphene-boron nitride-graphene tunneling devices were measured using scanning photocurrent microscopy. A confocal microscopy setup was used to focus a laser onto the sample surface while measuring the current produced at the contact electrodes. Using a piezoelectric mirror, the laser position could be moved across the device, allowing us to produce images of the tunneling current generated as a function of laser position. The sample itself was contained in an optical cryostat under high vacuum. Using liquid helium, the temperature could be regulated from room temperature down to  $\sim 4\text{K}$ . Vacuum feedthroughs provided electronic access to contacts on the device in order to apply voltages and measure currents on the sample.

The laser source was a broadband, pulsed supercontinuum laser coupled to a monochromator. Using this system the wavelength of the light could be varied between approximately  $450\text{nm}$  ( $2.75\text{eV}$ ) and  $2000\text{nm}$  ( $0.62\text{eV}$ ), allowing us to measure photocurrent produced as a function of photon energy. The laser was passed through a confocal microscopy setup, focusing the beam onto the sample while allowing the position to be varied. Lastly, an optical chopper was used in tandem with a lock-in amplifier to isolate the photocurrent signal and improve the signal-to-noise ratio. A schematic of the measurement setup is shown in Figure 5-1.

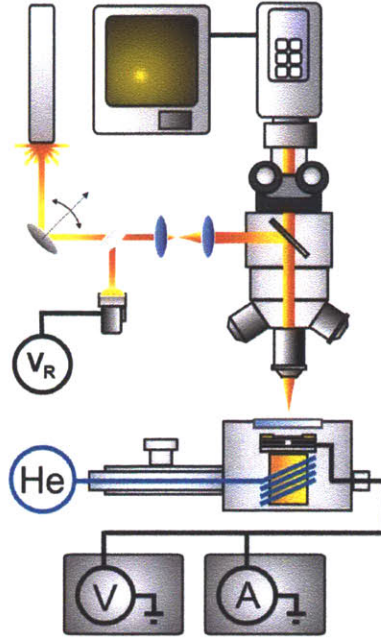


Figure 5-1: A schematic of the experimental apparatus, showing the broadband laser, the scanning mirror, the confocal microscope, and the liquid helium cryostat.

## 5.2 Resistance Characteristics

The resistance characteristics of both the source and drain graphene electrodes were measured using a two-probe geometry as a function of a gate voltage,  $V_G$ , applied to the other graphene sheet. A constant voltage was applied to one side of the graphene, while measuring the current produced at the other side. Dividing the two values provided a measure of the resistance. As shown in Figure 5-2 for typical devices, both the exfoliated graphene source and CVD graphene drain exhibited Dirac peaks (peaks in the resistance stemming from the reduced charge carrier density when the samples were gated to the charge neutrality point). The narrowness and symmetry of the exfoliated peak implies a much higher carrier mobility than the CVD drain, as is expected for CVD samples. The proximity of the charge neutrality points to  $V_G = 0V$  implies that there is minimal extrinsic doping of either the exfoliated or CVD-grown graphene sheets.



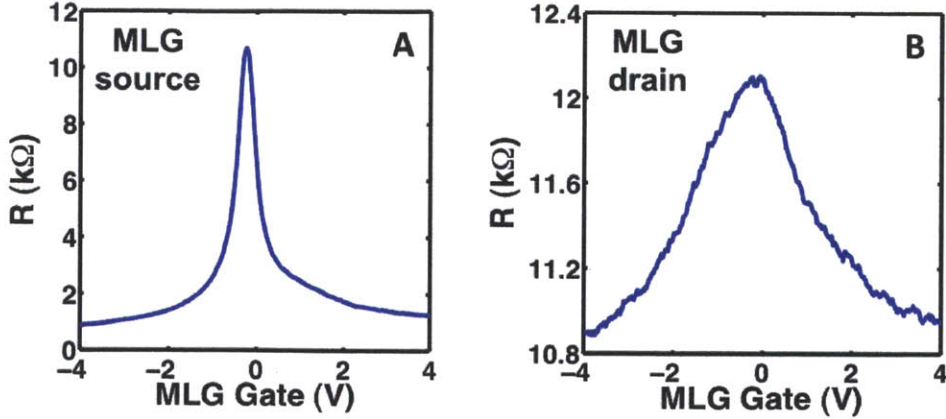


Figure 5-2: Resistance characteristics of the graphene source (A) and drain (B) electrodes. Both show a Dirac peak around 0V, implying that extrinsic doping is low.

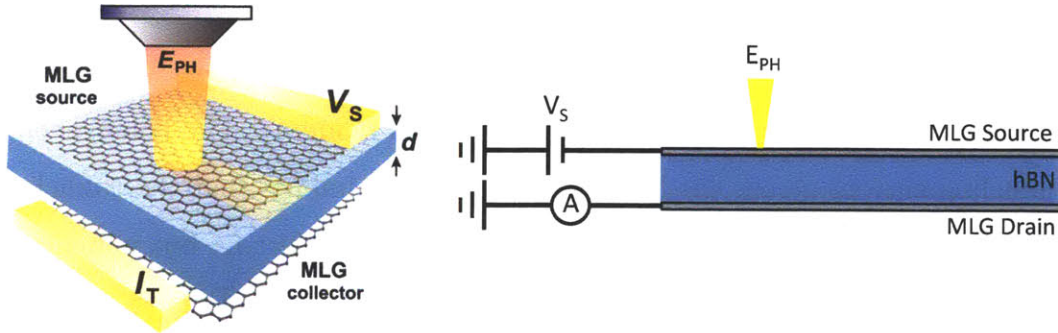


Figure 5-3: A schematic showing the geometry used for tunneling measurements. Tunneling current is collected at the graphene drain while bias is applied to the source and the laser is focused onto the sample.

### 5.3 Tunneling Measurements

To probe electronic transport across the boron nitride tunneling barrier, a voltage,  $V_S$ , was applied to the graphene source electrode, and the tunneling current,  $I$ , was measured at the graphene drain electrode. This measurement geometry is shown in Figure 5-3. Figure 5-4 shows a typical photocurrent image, obtained by scanning the laser across the device at a wavelength of 600nm and power of  $100\mu W$  at  $V_S = 0.5V$ . When the laser spot is far from the MLG source electrode, but still on the boron nitride and MLG drain, no discernible tunneling current is detected. When the laser moves onto the MLG source, such that it is above all three layers, a significant tunneling current of  $I \sim 600pA$  is measured in the drain electrode and is homoge-

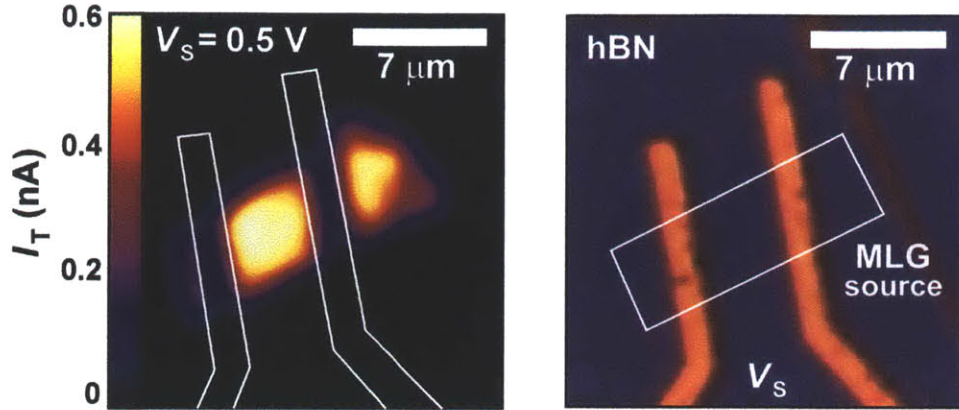


Figure 5-4: A photocurrent image showing the tunneling current measured at the graphene drain as a function of laser position. The active region of the device aligns exactly with the position of the graphene source electrode.  $\lambda = 600\text{nm}$ ,  $P = 100\mu\text{W}$ ,  $T = 100\text{K}$ ,  $V_S = 0.5\text{V}$ .

neously detected across the entire MLG source area ( $\sim 30\mu\text{m}$ ). The homogeneity of the tunneling current across the MLG source electrode implies that the tunneling is not coming from a localized defect in the boron nitride dielectric, but is instead an inherent property of the material itself.

Current-voltage characteristics were measured by fixing the laser at a specific spot above the MLG source, hBN, and MLG drain electrode, and varying the voltage applied to the source. This measurement was first performed in the dark (with the laser off). For a boron nitride thickness of 14nm at a temperature of 100K, as shown in Figure 5-5, no tunneling current was measured for bias voltages of up to  $V_S = \pm 8.5\text{V}$ . Based on this data, a minimum off-state resistance of  $\sim 1\text{T}\Omega$  was calculated, which is in-line with other measurements performed using this thickness of hBN [20].

In contrast to the dark tunneling characteristics, the illuminated  $I - V_S$  curve shown in Figure 5-5 exhibited a large tunneling current and asymmetric dependence on bias voltage. The current was found to increase rapidly with bias for both positive and negative voltages, but increased much more rapidly on the positive voltage side. In order to obtain the photon energy dependence of the photocurrent response,  $I - V_S$  curves were measured while slowly varying the wavelength of the incoming light from 480nm(2.58eV) to 700nm(1.77eV). As shown in Figure 5-6, two very different

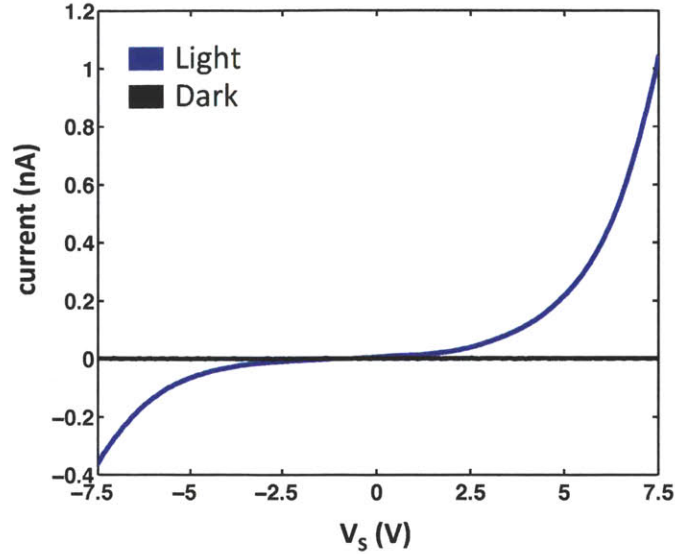


Figure 5-5: The tunneling current measured as a function of bias voltage with the laser fixed on the region of highest photoresponse. No tunneling is observed with the laser off, but a large, asymmetric tunneling current is observed with the laser on.

behaviors were observed for positive and negative voltages. On the negative bias side, the tunneling current was found to increase monotonically in both photon energy and bias voltage (see Figure 5-7A). On the positive bias side, however, the tunneling current was found to exhibit a peak in photon energy which dispersed in bias voltage. As the bias voltage increased, the peak was observed to move to lower photon energies (see Figure 5-7B). This dispersion implies that the observed behavior stems from a property of the device itself, and is not simply caused by a fluctuation in the light intensity or a peak in the material's absorption spectrum.

These measurements were analyzed using the Fowler-Nordheim tunneling model described in Section 3.2, with one important caveat. When a bias is applied to the graphene source layer, it not only serves to tilt the hBN's band structure and therefore the potential energy barrier, but it also serves to dope the graphene sheets via capacitive coupling. If we have two graphene sheets separated by only a thin-film insulating layer, then applying an electric field between the sheets will induce charge carriers, changing the carrier concentration in each sheet. The carrier concentration

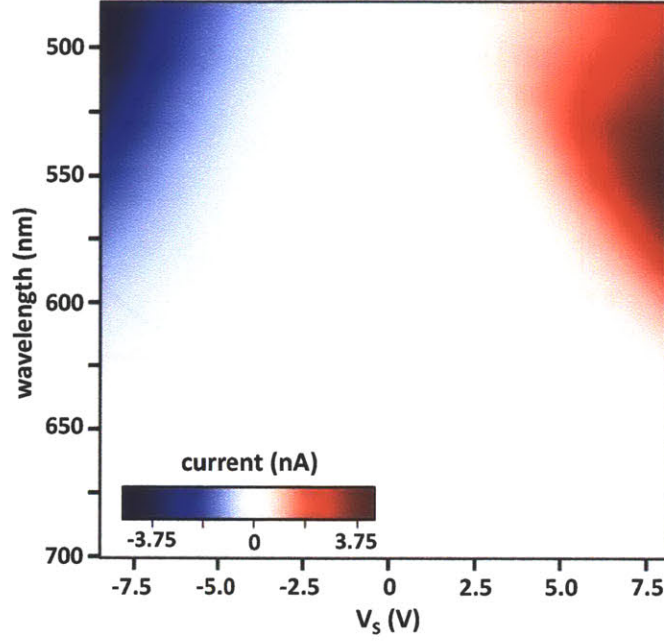


Figure 5-6: The tunneling current measured at the graphene drain plotted against photon wavelength (energy) and bias voltage. An asymmetric behavior is observed between the negative and positive bias regions, with the tunneling current exhibiting a sharp peak in photon energy for positive biases.

in each sheet is given by

$$\epsilon F_b = 4\pi n_B e \quad (5.1)$$

$$-\epsilon F_b = 4\pi n_T e \quad (5.2)$$

where  $\epsilon$  is the dielectric constant of the insulating material,  $F_b$  is the applied electric field, and  $n_B$  ( $n_T$ ) is the carrier density in the bottom (top) layer of graphene [4]. Combining Eq. (5.1) and Eq. (5.2) yields the condition that  $n_B = -n_T$ . A second condition can be derived from conserving energy as a test charge is moved from one sheet to the other. This condition is given by

$$eV_b = eF_b t - \mu(n_T) + \mu(n_B) \quad (5.3)$$

where  $V_b$  is the bias voltage applied between the two sheets,  $t$  is the thickness of the insulator, and  $\mu(n_{T/B})$  is the change in the chemical potential in each of the

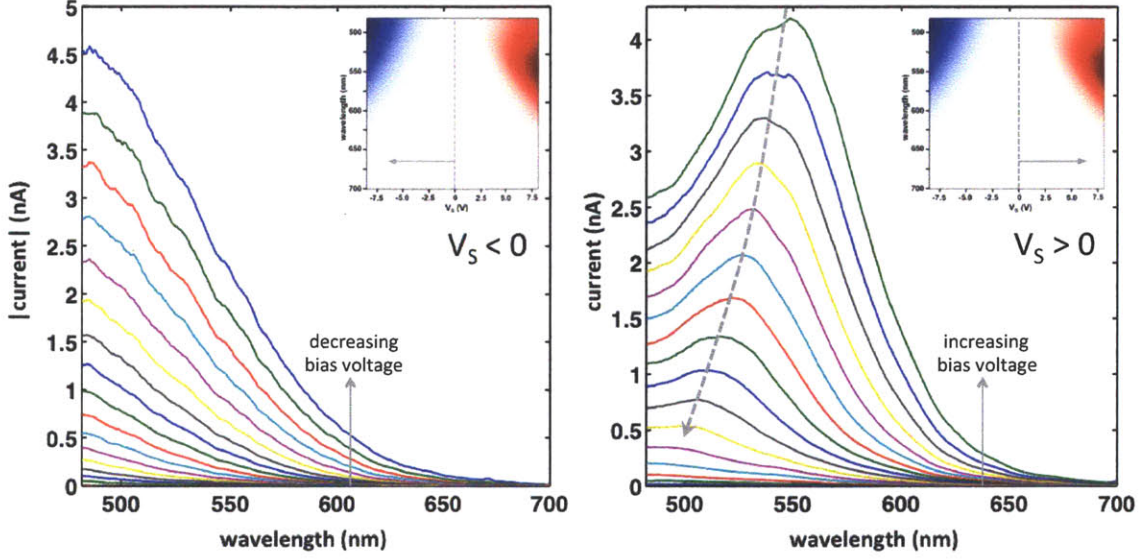


Figure 5-7: Line cuts of the tunneling current measured as a function of photon wavelength (energy) at negative (left) and positive (right) bias voltages. At negative voltages the tunneling current grows monotonically in photon energy. At positive positive voltages, however, the tunneling current exhibits a peak which disperses in bias voltage.

graphene sheets [4]. This change in chemical potential is represented as a shift of the conical Dirac band structure with respect to the insulator band structure (see Figure 5-8). Replacing  $eF_b t$  in Eq. (5.3) with an expression for the classical capacitance of a tunnel barrier, and taking into account electron-hole symmetry in graphene ( $\mu(-n) = -\mu(n)$ ), Eqs. (5.1, 5.2, 5.3) can be reduced to

$$\frac{4\pi e^2 t}{\epsilon} n_T + 2\mu(n_T) + eV_b = 0 \quad (5.4)$$

In graphene,  $\mu(n) \sim \sqrt{n}$ , which means that Eq. (5.4) can be solved for  $n_T$ , and therefore  $\mu(n_T)$  and  $\mu(n_B)$  [5]. Thus, given an applied bias  $V_b$ , one can solve for the shifting of the Dirac cones with respect to the insulator in this model graphene-insulator-graphene system.

The system that is actually being measuring, however, is slightly more complex. In addition to graphene-hBN-graphene, there is a conductive back gate built into the silicon oxide wafer. During measurements, this back gate was kept at zero potential

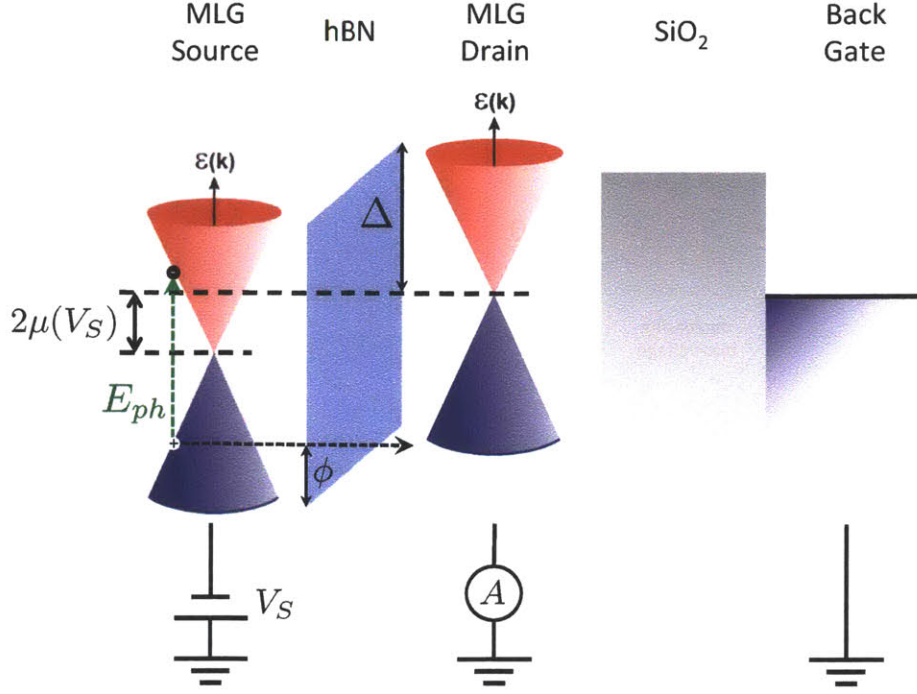


Figure 5-8: Schematic showing the shift induced in the Dirac cone of the source electrode when a voltage,  $V_S$ , is applied. The presence of a grounded back gate pins the graphene drain, forcing all the shifting to occur in the graphene source.

(grounded), as was the bottom layer of graphene (corresponding to the graphene drain electrode) via the amplifier. This meant that the charge neutrality point of the graphene drain did not move with respect to the valence band edge of the hBN (i.e. the Dirac cone did not shift). The difference in chemical potentials between the two layers, however, must still be conserved and is governed by Eq. (5.4). Therefore, if the bottom graphene layer (drain electrode) does not shift, then the top graphene layer (source electrode) must shift by twice as much,  $2\mu(n_T)$ , where  $\mu(n_T)$  is solved for using Eq. (5.4). What we end up with is a system where the Dirac cone of the graphene drain electrode does not shift when a bias is applied, but the Dirac cone of the graphene source electrode does.

In order to begin analyzing the data, we start with the simpler, negative bias region of Figure 5-6, where the tunneling current increases monotonically with bias voltage and photon energy. Based on previous results studying tunneling in graphene-hBN heterostructures, we assume that the tunneling observed here is mediated by

positive charge carriers (holes) [4]. If this is the case, then the negative tunneling current observed at negative biases corresponds to charge carriers tunneling from the graphene drain to the graphene source electrode. Since these are photo-excited charge carriers, and the Dirac cone of the graphene drain is fixed with respect to the hBN when biased, the energy for each of these charge carriers will be simply  $E_{ph}/2$ , where  $E_{ph}$  is the photon energy. The factor of 1/2 arises from the fact that, in graphene, electron-hole pairs are symmetrically excited about the charge neutrality point, each receiving half of a photon's energy. This means that if the intrinsic offset between the top of the valence band in boron nitride and the charge neutrality point in graphene is  $\Delta$ , then the effective barrier height for tunneling charges will be  $\phi = \Delta - E_{ph}/2$ .

In order to extract the effective barrier height,  $\ln(I(V)/V^2)$  was plotted against  $1/V$  for various photon energies, as shown in Figure 5-9A. Tunneling theory predicts that  $I - V_S$  curves at fixed photon energies should be linear on this plot. The  $I - V_S$  curves were therefore fit to lines and the slopes of those lines were extracted. This term, which we denote  $\beta$ , has the following form from Eq. (3.8)

$$\beta = \frac{4t\sqrt{2m^*}\phi^{3/2}}{3e\hbar} \quad (5.5)$$

where  $t$  is the thickness of the boron nitride layer,  $m^*$  is the effective mass of charge carriers in the boron nitride, and  $\phi$  is the effective barrier height for photo-excited charge carriers. This means that  $\beta^{2/3} \sim \phi$ , and since  $\phi$  is linear in photon energy,  $\beta^{2/3}$  should be as well. Figure 5-9B shows  $\beta^{2/3}$  plotted against  $E_{ph}$ , and the data is indeed very linear. Moreover, at the point where  $\beta^{2/3}$  intersects the x-axis,  $\phi = 0$ , which means that  $E_{ph}/2 = \Delta$ . The x-intercept was extracted using a linear fit and was found to occur at  $E_{ph} = 2.70\text{eV}$ , which corresponds to an intrinsic barrier height of  $\Delta = 1.35\text{eV}$ .

Once the intrinsic barrier height is known, Figure 5-9B can also be used to extract the effective mass of charge carriers tunneling through the hBN layer. From Eq. (5.5),  $\beta^{2/3}$  is linear in  $E_{ph}$  and the linear coefficient only involves  $m^*$  and known constants such as the thickness of the hBN and the electron charge. Therefore, extracting the

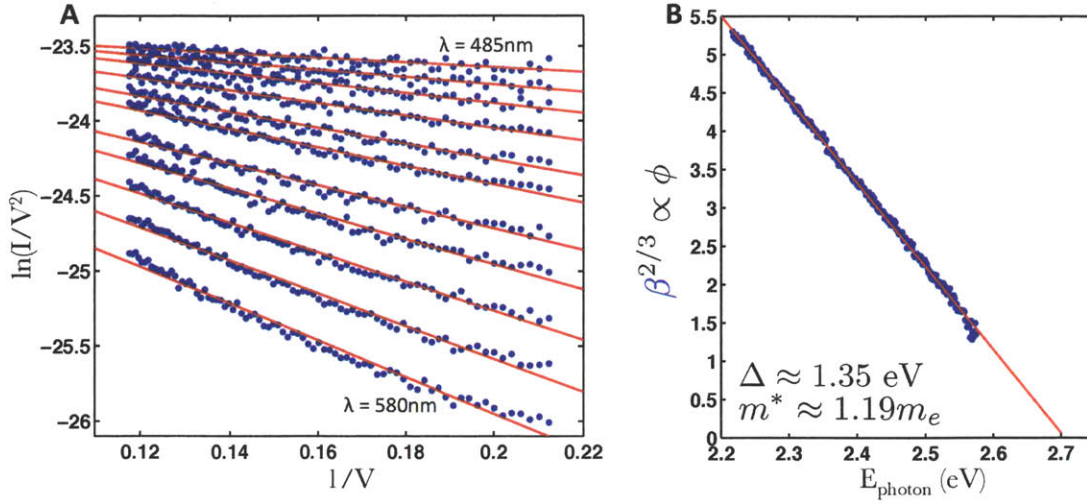


Figure 5-9: (A) A Fowler-Nordheim plot showing  $\ln(I(V)/V^2)$  plotted against  $1/V$  for various photon wavelengths. Blue dots represent data and red lines represent linear fits. (B) The linear coefficient extracted from the fits in (A) plotted to the two-thirds power. The intrinsic barrier height and effective carrier mass can be extracted from the x-intercept and slope of this line.

slope of  $\beta^{2/3}$  provides a measure of  $m^*$ , the effective mass. Using this method, the effective mass of tunneling charge carriers in the hBN was found to be  $m^* = 1.19m_e$ , where  $m_e$  is the free electron mass.

The positive bias side of Figure 5-6 is a little more complicated than what was observed for negative voltages. There is a very clear peak in the tunneling current, which becomes even more apparent when the differential conductance,  $(dI/dV_S)$ , is plotted instead (Figure 5-10A). Assuming that tunneling is still dominated by holes, the tunneling current in positive bias corresponds to charge carriers tunneling from the graphene source electrode to the graphene drain electrode. Because electron-hole pairs in graphene are excited symmetrically about the charge neutrality point of the graphene source, the energy of these photo-excited charge carriers will be  $E_{ph}/2 - 2\mu(n_T)$ , where  $2\mu(n_T)$  is the shift of the charge neutrality point and is given by Eq. (5.4). This means that the effective barrier height encountered by tunneling charge carriers will be  $\phi = \Delta - E_{ph}/2 - 2\mu(n_T)$ .

Since the effective barrier height,  $\phi$ , now depends on the bias voltage, a plot of  $\ln(I(V)/V^2)$  against  $1/V$  will no longer be linear and the photon-energy dependence



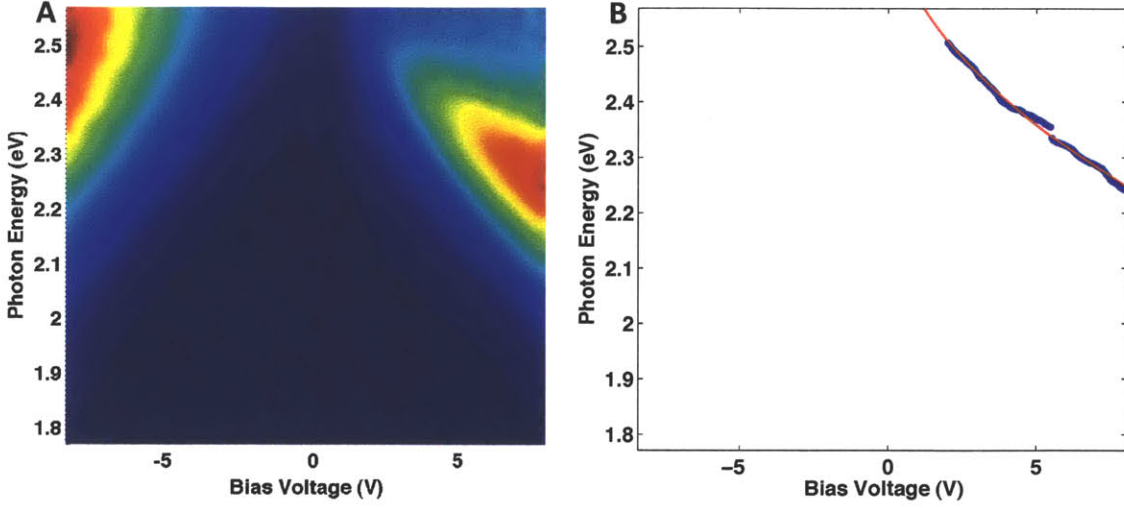


Figure 5-10: (A) The differential conductance,  $dI/dV_S$ , of the tunneling current plotted as a function of photon energy and bias voltage. (B) The position of the positive bias conductance peaks as a function of photon energy and bias voltage. The red line represents the fit to Eq. (5.6).

cannot be easily extracted. Instead, we use the position of the conductance peak to try and determine the intrinsic barrier height. When the energy of a photo-excited carrier is less than the intrinsic barrier, it will tunnel through the insulator via Fowler-Nordheim tunneling. If the energy of the carrier is greater than the barrier height, however, there will be no tunneling involved and it will travel through the valence band of the insulator via diffusive transport. In this regime, the behavior will be ohmic and the conductance of the  $I - V_S$  curves will saturate to some constant value. As the carrier energy approaches the intrinsic barrier height,  $\phi \rightarrow 0$  and the Fowler-Nordheim tunneling expression diverges. This means that the maximum conductance will occur where  $\phi = \Delta - E_{ph}/2 - 2\mu(n_T) = 0$ . Solving Eq. (5.4) for  $\mu(V_S)$  and rearranging, one finds that

$$E_{ph} = 2(\Delta - 2\mu(V_S)) \quad (5.6)$$

This is the condition that must be satisfied along the conductance peak in positive bias.

Figure 5-10B shows the position of the positive bias conductance peak. The peak position was extracted line-by-line from the original dataset and plotted as a function

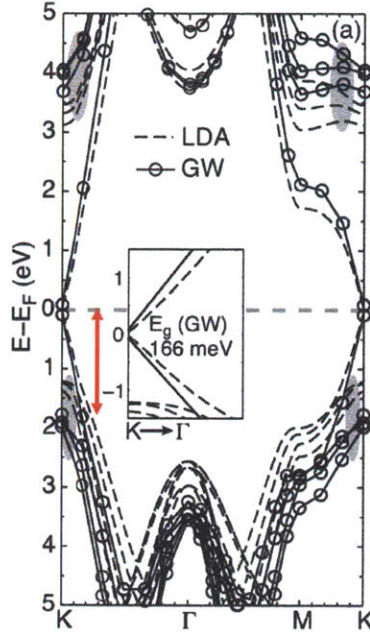


Figure 5-11: Theoretical calculations of the hBN-graphene interface. The red arrow marks the separation between the top of the hBN valence band the charge neutrality point in graphene, which is predicted to be between 1.25 – 2.00 eV. (Image adapted from [21].)

of bias voltage. Eq. (5.6) was fit to the extracted peak to find the intrinsic barrier height, which was found to be  $\Delta = 1.38\text{eV}$ , in close agreement with the barrier height that was determined from the negative bias data.

## 5.4 Comparison to Theory

Using the spectroscopic tunneling previously described we were able to extract values for the intrinsic offset between the valence band in hBN and the charge neutrality point in graphene, and the effective mass of tunneling charge carriers in hBN. From the negative and positive bias data, the band offset was found to be 1.35eV and 1.38eV, respectively. Theoretical calculations of the graphene-hBN interface show that the band offset should lie in the range of 1.25 – 2.00eV (see Figure 5-11), which is in very good agreement with values observed here [21].

Using the negative bias data, a value for the effective mass of charge carriers in hBN was also measured and was found to be  $1.19m_e$ . Theoretical calculations of

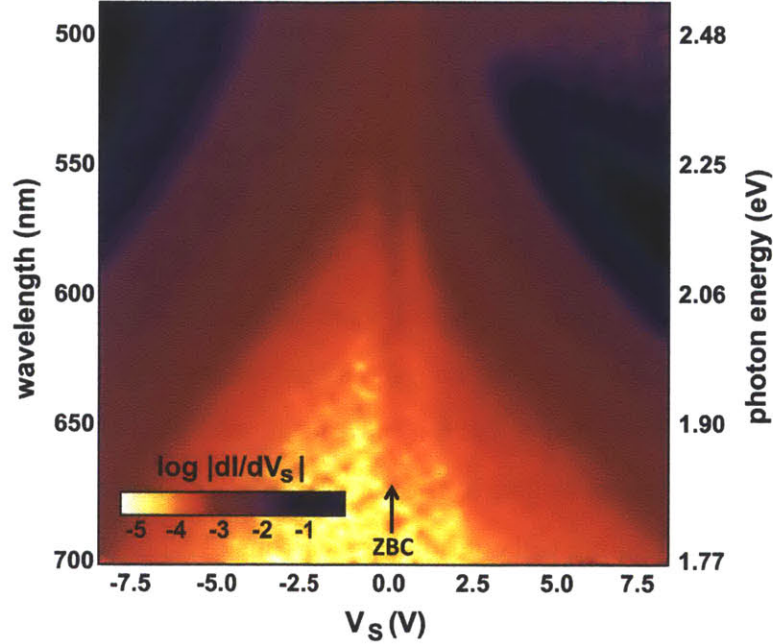


Figure 5-12: The tunneling conductance,  $dI/dV_S$ , plotted on a logarithmic scale, showing a peak at zero bias. This peak persists across a broad range of photon energies.

the hBN band structure show that holes traveling in the  $M - L$  direction (the same direction in which the tunneling occurs) should have an effective mass of  $1.33m_e$  [9]. This agrees well with what was observed and is consistent with our initial assumption that tunneling was dominated by holes. For comparison, the effective mass of electrons in the  $M - L$  direction is  $2.21m_e$ , much larger than what was measured. The slight discrepancy between the theoretically calculated mass for holes and the measured mass could be due to impurities, which scatter carriers into the plane where the effective mass is lower than  $1.33m_e$ .

## 5.5 Zero Bias Conductance

So far, using Fowler-Nordheim theory, we have only considered the high-bias tunneling properties of these graphene-hBN heterostructure devices. Looking carefully at the conductance data plotted in Figure 5-10, however, one notices that there is a slight peak in the conductance located at zero bias. This peak becomes much more apparent

when the conductance is plotted on a logarithmic scale, as has been done in Figure 5-12. This peak seems to persist for a broad range of photon energies and is surprising because Fowler-Nordheim tunneling predicts that the conductance at zero bias should be zero. This implies that some secondary tunneling mechanism is present, which dominates at low bias.

One candidate for this tunneling mechanism is thermionic emission. Thermionic emission is the mechanism by which charge carriers can be thermally excited over a potential barrier. Because charge carriers are fermions, they will equilibrate into a Fermi energy distribution at some given temperature,  $T$ . The Fermi distribution has the property that it has a long tail containing electrons of higher-than-average energy. Thus, if the average electron energy is  $kT$ , the tail will contain a small number of electrons with energies exceeding  $kT$ . Some of these excited electrons will have more energy than the barrier height and will conduct. This process is known as thermionic emission. As the temperature increases, the number of electrons in the Fermi tail will increase and therefore the number of electrons conducting over the barrier will also increase.

In graphene, electrons exhibit a very strong hot-carrier effect. Exciting the electronic system using light is known to create an out-of-equilibrium electron distribution at an elevated temperature compared to the lattice [13]. This hot distribution is the result of a bottleneck in the acoustic phonon relaxation pathways, which is enhanced close to the charge neutrality point. Therefore, one would expect that the electrons are the hottest when the applied voltage is zero, since that is when the graphene sheets are doped to their charge neutrality points. If thermionic emission is indeed the current generating mechanism, then one would expect it to peak at low bias, since that is when the electronic temperature is highest. This is exactly what is observed in the conductance data.

# Chapter 6

## Conclusions

In conclusion, graphene-boron nitride-graphene heterostructures were fabricated to observe photon-induced tunneling through the boron nitride. We observed that in the presence of light, a large tunneling current could be observed in these devices and this tunneling current was strongly dependent on bias voltage and photon energy. For negative bias voltages, the tunneling current was found to be monotonic, but for positive bias voltages a peak was observed at certain photon energies, which dispersed in bias voltage. These high-bias behaviors were found to fit well to a Fowler-Nordheim tunneling model and enabled us to extract values for the band offset between graphene and hBN and effective mass of charge carriers in the hBN. The intrinsic offset between the top of the valence band in hBN and the charge neutrality point in graphene was found to be  $\sim 1.36\text{eV}$  and the effective mass for holes tunneling through hBN was found to be  $\sim 1.19m_e$ . Both values agree well with theoretical calculations.

Additionally, we observed the presence of a peak in the conductance at zero applied bias. We believe that this peak is the result of thermionic emission caused by the elevated electronic temperature near the charge neutrality points in the graphene electrodes. If so, then this peak is a result of the hot-carrier effect in graphene and might provide a way to directly measure the associated relaxation timescales.

This work has shown that tunneling graphene-insulator-graphene heterostructures can be greatly enhanced by the presence of light, opening the possibility of using these types of materials in photodetector applications where low noise and high sensitivity

are needed. Different materials, such as molybdenum disulfide or tungsten diselenide, might have higher or lower band offsets than boron nitride, providing devices that are sensitive in different regions of the electromagnetic spectrum. Moreover, what we have demonstrated here, photon-induced tunneling, is a new spectroscopic tool that could be used to measure other atomically thin materials and extract properties about their interfaces.

# Bibliography

- [1] P. R. Wallace. The Band Structure of Graphite. *Phys. Rev.*, **71**(9), 622-634, 1947.
- [2] K. S. Novoselov, A. K. Geim, S. V. Morozov, D. Jiang, Y. Zhang, S. V. Dubonos, I. V. Grigorieva, and A. A. Firsov. Electric Field Effect in Atomically Thin Carbon Films. *Science*, **306**(5696), 666-669, 2004.
- [3] C. R. Dean, A. F. Young, I. Meric, C. Lee, L. Wang, S. Sorgenfrei, K. Watanabe, T. Taniguchi, P. Kim, K. L. Shepard, and J. Hone. Boron nitride substrates for high-quality graphene electronics. *Nature Nano.*, **5**, 722-726, 2010.
- [4] L. Britnell, R. V. Gorbachev, R. Jalil, B. D. Belle, F. Schedin, A. Mishchenko, T. Georgiou, M. I. Katsnelson, L. Eaves, S. V. Morozov, N. M. R. Peres, J. Leist, A. K. Geim, K. S. Novoselov, and L. A. Ponomarenko. Field-Effect Tunneling Transistor Based on Vertical Graphene Heterostructures. *Science*, **335**(6071), 947-950, 2012.
- [5] A. H. Castro Neto, F. Guinea, N. M. R. Peres, K. S. Novoselov, and A. K. Geim. The electronic properties of graphene. *Rev. Mod. Phys.*, **81**(1), 109-162, 2009.
- [6] A. K. Geim and K. S. Novoselov. The rise of graphene. *Nature Mat.*, **6**, 183-191, 2009.
- [7] K. S. Novoselov, A. K. Geim, S. V. Morozov, D. Jiang, M. I. Katsnelson, I. V. Grigorieva, S. V. Dubonos, and A. A. Firsov. Two-dimensional gas of massless Dirac fermions in graphene. *Nature*, **438**, 197-200, 2005.
- [8] A. F. Young and P. Kim. Quantum interference and Klein tunnelling in graphene heterojunctions. *Nature Phys.*, **5**, 222-226, 2009.
- [9] Y. N. Xu and W. Y. Ching. Calculation of ground-state and optical properties of boron in the hexagonal, cubic, and wurtzite structures. *Phys. Rev. B*, **44**(15), 7787-7798, 1991.
- [10] H. Wang, T. Taychatanapat, A. Hsu, K. Watanabe, T. Taniguchi, P. Jarillo-Herrero, and T. Palacios. BN/Graphene/BN transistors for RF applications. *IEEE Elec. Dev. Lett.*, **32**, 1209-1211, 2011.
- [11] F. Bonaccorso, Z. Sun, T. Hasan, and A. C. Ferrari. Graphene photonics and optoelectronics. *Nature Photon.*, **4**, 611-622, 2010.

- [12] K. F. Mak, L. Ju, F. Wang, and T. F. Heinz. Optical spectroscopy of graphene: From the far infrared to the ultraviolet. *Solid State Comm.*, **152**(15), 1341-1349, 2012.
- [13] N. M. Gabor, J. C. W. Song, Q. Ma, N. L. Nair, T. Taychatanapat, K. Watanabe, T. Taniguchi, L. S. Levitov, P. Jarillo-Herrero. Hot carrier-assisted intrinsic photoresponse in graphene. *Science*, **334**(6056), 648-652, 2011.
- [14] R. T. Ross and A. J. Nozik. Efficiency of hot-carrier solar energy converters. *J. Appl. Phys.*, **53**, 3813-3818, 1982.
- [15] J. W. Schwede, I. Bargatin, D. C. Riley, B. E. Hardin, Samuel J. Rosenthal, Y. Sun, F. Schmitt, P. Pianetta, R. T. Howe, Z. X. Shen, and N. A. Melosh. Photon-enhanced thermionic emission for solar concentrator systems. *Nature Mat.*, **9**, 762-767, 2010.
- [16] G. Gamow. Zur Quantentheorie des Atomkernes. *Z. Physik*, **51**, 204-212, 1928.
- [17] R. H. Fowler and L. Nordheim. Electron Emission in Intense Electric Fields. *Proc. Roy. Soc.*, **119**(781), 173-181, 1928.
- [18] P. Y. Huang, C. S. Ruiz-Vargas, A. M. van der Zande, W. S. Whitney, M. P. Levendorf, J. W. Kevek, S. Garg, J. S. Alden, C. J. Hustedt, Y. Zhu, J. Park, P. L. McEuen, and D. A. Muller. Grains and grain boundaries in single-layer graphene atomic patchwork quilts. *Nature*, **469**, 389-392, 2011.
- [19] J. C. Koepke, J. D. Wood, D. Estrada, Z. Y. Ong, K. T. He, E. Pop, and J. W. Lyding. Atomic-Scale Evidence for Potential Barriers and Strong Carrier Scattering at Graphene Grain Boundaries: A Scanning Tunneling Microscopy Study. *ACS Nano*, **7**(1), 75-86, 2013.
- [20] G. H. Lee, Y. J. Yu, C. Lee, C. Dean, K. L. Shepard, P. Kim, and J. Hone. Electron tunneling through atomically flat and ultrathin hexagonal boron nitride. *Appl. Phys. Lett.*, **99**, 243114, 2011.
- [21] N. Kharche and S. K. Nayak. Quasiparticle Band Gap Engineering of Graphene and Graphone on Hexagonal Boron Nitride Substrate. *Nano Lett.*, **11**(12), 5274-5278, 2011.